
NEURAL VORTEX METHOD: FROM FINITE LAGRANGIAN PARTICLES TO INFINITE DIMENSIONAL EULERIAN DYNAMICS

Shiying Xiong *

Department of Computer Science
Dartmouth College
Hanover, NH 03755

Xingzhe He

Department of Computer Science
Dartmouth College
Hanover, NH 03755

Yunjin Tong

Department of Computer Science
Dartmouth College
Hanover, NH 03755

Bo Zhu

Department of Computer Science
Dartmouth College
Hanover, NH 03755

June 9, 2020

ABSTRACT

In the field of fluid numerical analysis, there has been a long-standing problem: lacking of a rigorous mathematical tool to map from a continuous flow field to discrete vortex particles, hurdling the Lagrangian particles from inheriting the high resolution of a large-scale Eulerian solver. To tackle this challenge, we propose a novel learning-based framework, the Neural Vortex Method (NVM), which builds a neural-network description of the Lagrangian vortex structures and their interaction dynamics to reconstruct the high-resolution Eulerian flow field in a physically-precise manner. The key components of our infrastructure consist of two networks: a vortex representation network to identify the Lagrangian vortices from a grid-based velocity field and a vortex interaction network to learn the underlying governing dynamics of these finite structures. By embedding these two networks with a vorticity-to-velocity Poisson solver and training its parameters using the high-fidelity data obtained from high-resolution direct numerical simulation, we can predict the accurate fluid dynamics on a precision level that was infeasible for all the previous conventional vortex methods (CVMs). To the best of our knowledge, our method is the first approach that can utilize motions of finite particles to learn infinite dimensional dynamic systems. We demonstrate the efficacy of our method in generating highly accurate prediction results, with low computational cost, of the leapfrogging vortex rings system, the turbulence system, and the systems governed by Euler equations with different external forces.

1 Introduction

Accurately capturing and quantifying the motions of fluid with fine details has been a challenging task of fluid numerical analysis for centuries. From the theoretical standpoint, one of the most critical sets of governing equations of fluid dynamics is the Euler equations. Given a fluid velocity field $\mathbf{u}(\mathbf{x}, t)$ with an incompressible constraint, its underlying dynamics can be described by

$$\begin{cases} \frac{\partial \mathbf{u}}{\partial t} + (\mathbf{u} \cdot \nabla) \mathbf{u} = -\frac{1}{\rho} \nabla p + \mathbf{f}, \\ \nabla \cdot \mathbf{u} = 0, \end{cases} \quad (1)$$

where t denotes the time, p the pressure, ρ the density, and \mathbf{f} the body accelerations (per unit mass) acting on the continuum, for example gravity, inertial accelerations, electric field acceleration, and so on.

*corresponding author, email: shiying.xiong@dartmouth.edu

To computationally solve the Euler equations, many numerical methods are developed and among which the most widely used one is the conventional vortex methods (CVMs) [34]. CVMs enjoy several advantages such as its automatic adaptivity of the computational elements, the numerical conservation of physically conserved quantities, the ability to simulate phenomena covering many orders of magnitude, and the rigorous treatment of boundary conditions at infinity. CVMs are based on the discretization of the vorticity field $\boldsymbol{\omega} = \nabla \times \mathbf{u}$ and the Lagrangian description of the governing equations (1) that, when solved, determine the evolution of the computational elements. Specifically, discretizing the (1) with N particles results in a set of ordinary differential equations (ODEs) for the particle strengths $\boldsymbol{\Gamma} = \{\boldsymbol{\Gamma}_i | i = 1, \dots, N\}$ and the particle positions $\mathbf{X} = \{\mathbf{X}_i | i = 1, \dots, N\}$ as

$$\begin{cases} \frac{d\boldsymbol{\Gamma}_i}{dt} = \gamma_i(\boldsymbol{\Gamma}, \mathbf{X}), \\ \frac{d\mathbf{X}_i}{dt} = \mathbf{u}_i + \mathbf{v}_i(\boldsymbol{\Gamma}, \mathbf{X}). \end{cases} \quad (2)$$

Here, $\boldsymbol{\Gamma}_i$ is the integral of $\boldsymbol{\omega}$ over the i^{th} computational element, γ_i is the change rate of the particle strength due to the vortex stretching, $\mathbf{u}_i = \mathbf{u}(\mathbf{X}_i)$ is the velocity at \mathbf{X}_i , and \mathbf{v}_i is a drift velocity caused by the vorticity distribution and the external force [12].

However, the implementation of CVM faces a major challenge that is to model the right-hand sides (RHSs) of (2) based on (1). In the CVMs, the velocity $\mathbf{u}_i = \mathbf{u}(\mathbf{X}_i)$ on the RHSs of (2) is evaluated by the Biot–Savart law (BS law). If the volume of vortex element is not considered, \mathbf{u}_i can be calculated by

$$\mathbf{u}_i = \frac{1}{2(n_d - 1)\pi} \sum_{j \neq i}^N \frac{\boldsymbol{\Gamma}_j \times (\mathbf{X}_i - \mathbf{X}_j)}{|\mathbf{X}_i - \mathbf{X}_j|^{n_d}}, \quad (3)$$

where n_d is the dimension of the flow field. However, there are several drawbacks of using BS law. First, the assumption that the vortices are point-like largely limits the use of BS law. Second, the drift velocity \mathbf{v}_i due to the external force cannot be obtained using CVM without knowing the function of the external force. Even given the function, CVM still fails to capture \mathbf{v}_i accurately in most cases. Lastly, when there are two particles that are close enough, equation (3) will have a large error. All of the above problems make CVM inaccurate and inapplicable in solving the underlying fluid dynamics under many situations [7].

An alternative method, grid method, is developed to solve the accuracy issue that arises in the vortex method. Many researchers are devoted to high-resolution large-scale Eulerian solver [25, 5]. However, an unignorable problem of the grid method is its high computational cost that is sometimes unaffordable for realistic conditions.

To quantify the fluid dynamics accurately in an efficient manner, we propose a novel framework, Neural Vortex Method (NVM), that extracts information from the Eulerian specification of the flow field (or the images of flow visualizations) and translates it into knowledge about the underlying fluid field through physics-informed neural networks. Learning directly from high-dimensional observations, such as images, is unable to be achieved using traditional methods, since extracting the velocity and pressure fields directly from the images is challenging. We address this problem by constructing a vortex representation network (section 2.2 Detection Network) to identify the positions and the vorticity of Lagrangian vortices from a grid-based velocity field, which from a mathematical perspective connects (1) with (2). In this way, we simplify the vorticity field into a field only consists of the identified vortices. Given the detected vortices, we then use a vortex interaction network (section 2.3 Dynamics Network) to learn the underlying governing dynamics of these finite structures. Dynamics networks model the RHSs of 2 accurately under a variety of conditions, resolving the long-standing problem in CVM. To build a fully automated tool-chain that can construct a high-resolution Eulerian flow field from the Lagrangian inductive priors, we embed these two networks with a vorticity-to-velocity Poisson solver and trained its parameters using the high-fidelity data obtained from high-resolution direct numerical simulation. The model is trained only with information collected from the interaction of 2 to 6 vortices, and the trained model can be applied to any arbitrary vorticity field with any number of vortices.

We demonstrate the efficacy of our method in generating highly accurate prediction results, with low computational cost, of the leapfrogging vortex rings system, the turbulence system, and the systems governed by Euler equations with different external forces, that are challenging to model for CVMs. As a example, Figure 1 depicts the two-dimensional Lagrangian scalar fields at $t = 1$ with the initial condition $\phi = x$ and resolution 2000^2 . The evolution of the Lagrangian scalar fields are induced by $O(10)$ and $O(100)$ random NVM vortex particles. With a small number of NVM vortex particles, shown in Figure 1 (a), the spiral structure [26, 27] of individual NVM vortex particles can be observed clearly. With a large number of NVM vortex particles, the underlying field exhibits turbulent behaviors. Generally, the high-resolution results shown in Figure 1 can only be achieved by supercomputation using grid-based methods [46], while NVM allows these to be generated on any laptop with GPU. Although CVM does not require such a large computational cost as grid methods, suffering from inaccuracy, it can never produce such an accurate depiction of Lagrangian fields.

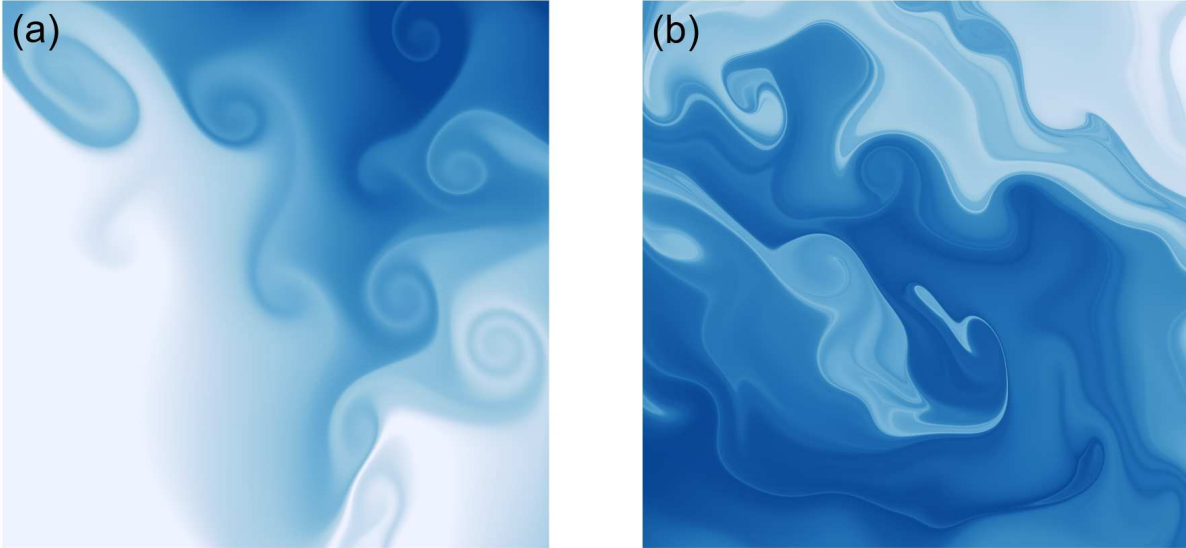


Figure 1: Two-dimensional Lagrangian scalar fields at $t = 1$ with the initial condition $\phi = x$ and resolution 2000^2 . The evolution of the Lagrangian scalar fields are induced by (a) $O(10)$ and (b) $O(100)$ random NVM vortex particles.

Using NVM as an alternative of the traditional vortex particle methods and grid-based methods has several benefits:

Accuracy NVM can predict the accurate fluid dynamics on a precision level that was infeasible for all the previous CVMs.

Efficiency Our method only requires training data collected from a very short window of training period (more than 100 times shorter than the prediction period). Compared with the grid-based methods, NVM can achieve the same level of accuracy with much lower computational cost.

Feasibility NVM can be applied to fluid fields with any number of vortices with or without volume and with any boundary condition. It can capture the dynamics of the fluid under the influence of external forces. Moreover, due to the short training period NVM requires, NVM can be applied to predict real systems that are hard to acquire data from.

Adaptivity NVM inherits the ability of automatically adapting the computational elements from CVM.

2 Methodology

The training process of NVM consists of 3 major steps: dataset generation, detection network training, and dynamics network training. We utilize data collected from randomly generated vortices and the corresponding vorticity fields to train the detection network. The direct numerical simulation (DNS) is used to calculate the evolution of the vorticity fields. We use the well-trained detection network to identify the positions and the vorticity of vortices from the initial and the evolved vorticity fields. This process is shown in Figure 2. The identified vortices are then used to train the dynamics network.

To predict the future flow, we use the trained detection network to simplify the vorticity field into a field only consists of the identified vortices. Given the detected vortices, we then use the dynamics network to learn the underlying governing dynamics of these finite structures.

2.1 Dataset Generation

We randomly sample 2 to 6 vortices and create the initial vorticity field through convolution with a Gaussian kernel $\sim \mathcal{N}(0, 0.01)$. This process is repeated for 2000 times to generate 2000 samples. DNS is performed to solve (1) in the periodic box using a standard pseudo-spectral method [32]. Aliasing errors are removed using the two-thirds truncation method with the maximum wavenumber $k_{\max} \approx N/3$. The Fourier coefficients of the velocity is advanced in time

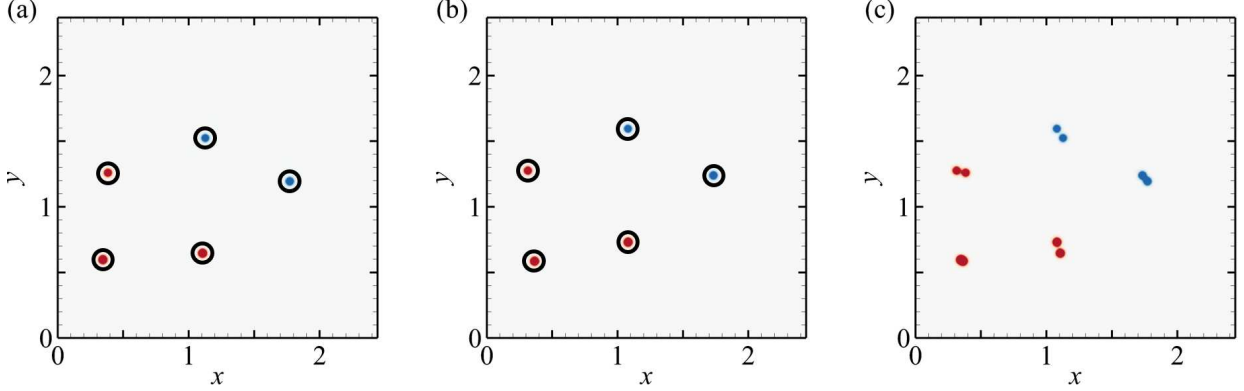


Figure 2: A example of vorticity contour at (a) $t = 0$, (b) $t = 0.2$, and (c) superposition of $t = 0$ and $t = 0.2$. The black circles indicate the location recognized by the detection network. The evolution from (a) to (b) is calculated by DNS.

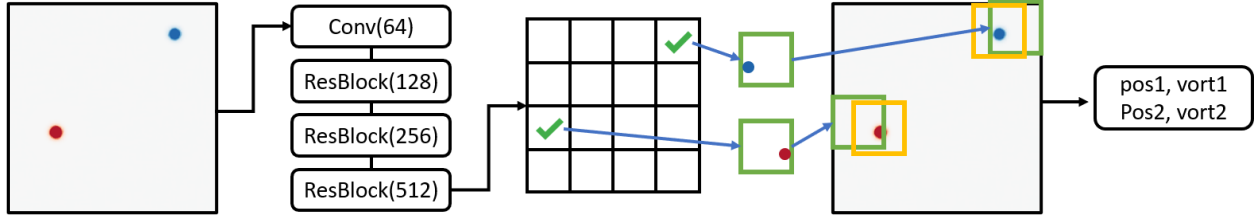


Figure 3: The architecture of the detection. It takes the vorticity field as input and output the position and vortex volume for each vortex detected. The *Conv* means the Conv2d-BatchNorm-ReLU combo and the *ResBlock* is the same as in [13]. In each *ResBlock*, we use stride 2 to downsample the feature map. The number in the parenthesis is the output dimension.

using a second-order Adams–Bashforth method, and the time step is chosen to ensure that the Courant–Friedrichs–Lewy number is less than 0.5 for numerical stability and accuracy. The pseudo-spectral method used in this DNS is similar to that described in [41, 42, 43, 44].

2.2 Detection Network

The input of the detection networks is a vorticity field of size $200 \times 200 \times 1$. As shown in Figure 3, we first feed the vorticity field into a small one-stage detection network and get the feature map of size $25 \times 25 \times 512$ (we downsampled 3 times). The primary reason for downsampling is to avoid extremely unbalanced data and multiple prediction for the same vortex. We then forward the feature map to 2 branches. In the first branch, we conduct a 1×1 convolution to generate a probability score \hat{p} of the possibility that there exists a vortex. If $\hat{p} > 0.5$, we believe there exists a vortex within the corresponding cells of the original $200 \times 200 \times 1$ vorticity field. In the second branch, we predict the relative position to the left-up corner of the cell of the feature map if the cell contains a vortex. Afterwards, we set a bounding box of 10×10 around these predicted vortices and use weighted average of the positions of the cells of the original vorticity field to find a exact position of the vortex. Finally, the vortex volume is calculated as the sum of the value of the cells in the bounding box normalized by the cell area.

Note that in the training process, we penalize the wrong position detection only if the cell that contains a vortex in the ground truth given by DNS is not detected. This idea is similar to [31]. We do not use the weighted average method to find the position in the training to ensure the detection network can produce detection results as accurate as possible. We use the focal loss [23] to further relief the unbalanced classification problem.

The main reason we use the detection network to generate training data for the dynamics network is that we want to use the high-resolution data generated by the method mentioned in 2.1 instead of by the approximate particle method (BS law). Moreover, there are many situations where BS law is inapplicable, discussed previously in the section 1. The detection network enables us to find the positions of the vortices accurately regardless of the situations.

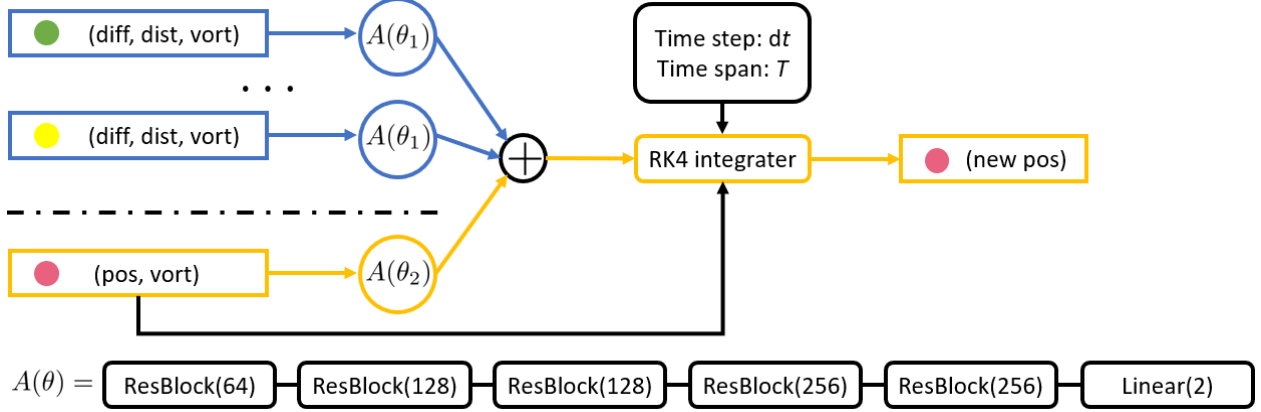


Figure 4: The architecture of the dynamics network. It takes the particles attribution as input and output the position for each vortex. The *ResBlock* has the same architecture as in [13] with the convolution layers replaced by linear layers. The number in the parenthesis is the output dimension.

The detection network is responsible for providing necessary information to the dynamics network. After the training process, we use the well-trained detection network to detect the vortices in the initial vorticity fields and the evolved vorticity field, both generated by the method in section 2.1. We then apply the nearest-neighbor method to pair the vortices detected in these two fields. Figure 2 shows the case of two fields at $t = 0$ and $t = 0.2$. The idea of nearest-neighbor pairing can be perceived from Figure 2 (c). The sample, or these two fields, is dropped if different numbers of vortices are detected in the initial and evolved fields or there exists large difference in the vorticity of paired vortices. The successfully detected vortices in the initial and evolved vorticity fields are passed together into the dynamics network for its training.

2.3 Dynamics Network

To learn the underlying dynamics of the vortices, we build a graph neural network similar to [2]. We predict the velocity of one vortex due to influences exerted by the other vortices and the external force, and use the fourth-order Runge–Kutta integrator to calculate the position in the next timestamp. As shown in Figure 4, for each vortex, we use a neural network $A(\theta_1)$ to predict the influences exerted by the other vortices and add them up. Specifically, for each vortex i , we consider the vortex j ($j \neq i$). The difference of their positions can be calculated by $\text{diff}_{ij} = \text{pos}_i - \text{pos}_j$, and their L2 distance is $\text{dist}_{ij} = \|\text{diff}_{ij}\|_2$. The input of the $A(\theta_1)$ is the vector $(\text{diff}_{ij}, \text{dist}_{ij}, \text{vort}_j)$ of length 4. Here, pos and vort are detected by the detection network. The output is the influence of the vortex j on the vortex i . In this way, we can calculate the influence of each vortex j ($j \neq i$) on the vortex i . We sum up the all the influences on the vortex i and treat the result as the influence exerted by the other vortices.

In addition, we use another neural network $A(\theta_2)$ to predict the global influence caused by the external force, which is determined by the vorticity and the position of the vortex. The input of $A(\theta_2)$ is a vector of length 3. The output is the influence exerted by the environment on the vortex i . Note that both the outputs of $A(\theta_1)$ and $A(\theta_2)$ are of length 2. Thus, we can add the two kinds of influence together, whose result is defined as the velocity of the vortex i . We feed the velocity into the fourth-order Runge–Kutta integrator to obtain the predicted position of vortex i . We assume the value of the vorticity is constant. In practice, the length of each time step used in the fourth-order Runge–Kutta integrator is 0.1s, and the total length is 0.2s.

3 Results

For both the detection network and the dynamics network, we use Adam optimizer [21] with learning rate $1e-3$. The learning rate decays every 20 epochs by a multiplicative factor of 0.8. For the detection network, we use a batch size of 32 and train it for 350 epochs. We use the cross entropy as the classification loss and use L1 loss for position prediction. To relief the unbalanced data problem in the detection network, we implement Focal loss [23] with $\alpha = 0.4$ and $\gamma = 2$. It takes 15 minutes to converge on a single Nvidia RTX 2080Ti GPU. For the dynamics network, we use a batch size of 64 and train it for 500 epochs. We use L1 loss for the position prediction. It takes 25 minutes to converge on a single Nvidia RTX 2080Ti GPU.

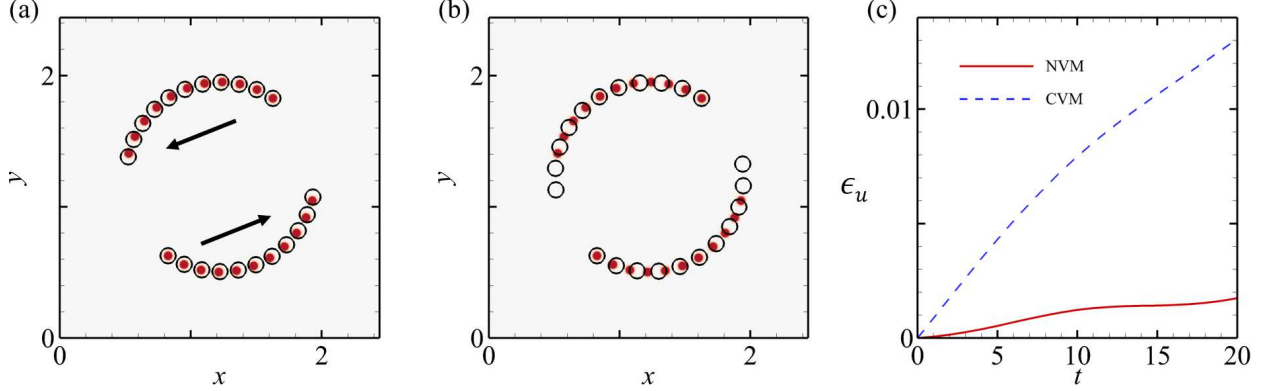


Figure 5: Comparison of NVM and CVM for solving Euler equation in the periodic box. (a) NVM, (b) CVM, and (c) The relative error of velocity in flow simulation. The red dots indicate the positions of 2 vortices at different time steps generated by DNS, and the black-circles in (a) and (b) are the prediction results of NVM and CVM, respectively. The black arrows indicate the directions of the motions of the 2 vortices.

3.1 NVM vs. CVM

To demonstrate that NVM is a better approach to capture the fluid dynamics than the traditional methods, we compare the prediction results made by NVM and CVM for solving Euler equations in the periodic box. We plot the results using NVM and CVM, and the relative error of velocity in the simulation in Figure 5 (a), (b), and (c) respectively. The red dots indicate the positions of 2 vortices at different time steps generated by DNS, and the black circles are the prediction results of NVM and CVM. It is quite obvious that in Figure 5 (a) the predictions made by NVM match the positions of vortices generated by DNS almost perfectly, while the predictions made by BS law in Figure 5 (b) contain a large error. The divergence of the relative error of velocity shown in Figure 5 (c) as t increases also shows that NVM outperforms the traditional methods by an increasing amount as the predicting period becomes longer.

3.2 Leapfrog and Turbulence

A classic example of interesting filament dynamics are the leapfrogging vortex rings, which is an axisymmetric laminar flow. This phenomenon is typically very hard to reproduce in standard fluid solver [6], especially to keep the symmetric structure. Here, we use NVM to predict the motions of 4 vortices and add 80000 randomly initialized tracers for better visualization. Since the tracers do not affect the dynamics of the underlying vorticity field, we use BS law to calculate the motions of these tracers for faster visualization. Figure 6 shows the evolution of the vorticity field predicted by NVM under the initial condition of leapfrogging vortex rings at $t = 0$, $t = 11$, $t = 22$, and $t = 33$. NVM accurately captures the symmetric structure of the leapfrogging vortex rings without losing such feature as time evolves.

Besides simple systems like leapfrogging vortex rings, NVM is capable of predicting complicated turbulence systems. Figure 1 depicts the two-dimensional Lagrangian scalar fields at $t = 1$ with the initial condition $\phi = x$ and resolution 2000^2 . The governing equation of the Lagrangian scalar fields is

$$\frac{\partial \phi}{\partial t} + \mathbf{u} \cdot \nabla \phi = 0. \quad (4)$$

The evolution of the Lagrangian scalar fields are induced by $O(10)$ and $O(100)$ random NVM vortex particles. Based on the particle velocity field from the NVM, a backward-particle-tracking method is applied to solve (4), and then the iso-contour of the Lagrangian field can be extracted as material structures in the evolution [46, 45, 47, 49, 48]. In Figure 1 (a), the spiral structure [26, 27] of individual NVM vortex particles can be observed clearly due to the small number of NVM vortex particles. In Figure 1 (b), the underlying field exhibits turbulent behaviors, since it is generated with a large number of NVM vortex particles. We demonstrate that NVM is capable of generating an accurate depiction of complex turbulence systems with low computational cost.

3.3 Euler equations with different external forces

In Figure 7, we show NVM's ability of stably making accurate predictions of fluid dynamics governed by Euler equations with different external forces, which are (a) $\mathbf{f} = \mathbf{0}$, (b) $\mathbf{f} = 0.05\omega(1, 0)$, and (c) $\mathbf{f} = 0.02\omega(\cos(x - x_c), -\sin(y - y_c))$. ω represents the vorticity, and (x_c, y_c) is the center of the computation domain. Here, we did not

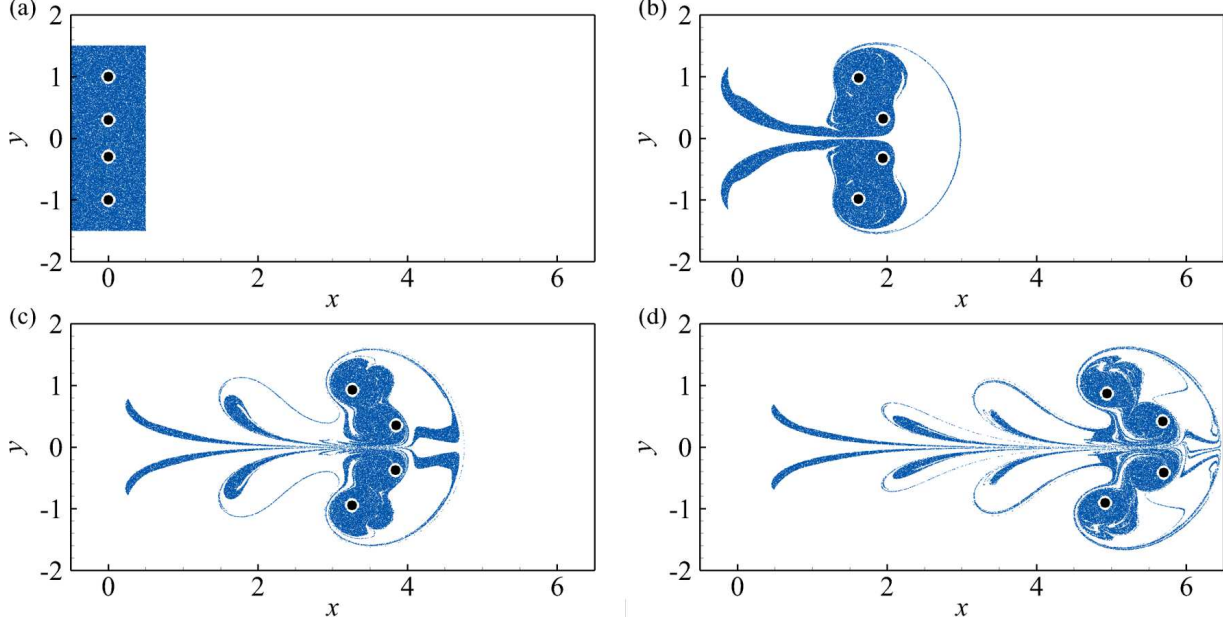


Figure 6: Vorticity field predicted by 4 NVM vortices under the initial condition of leapfrogging vortex rings at $t = 0$, $t = 11$, $t = 22$, and $t = 33$. Vortices are indicated by the white-black circles. For better visualization, we use 80000 tracers.

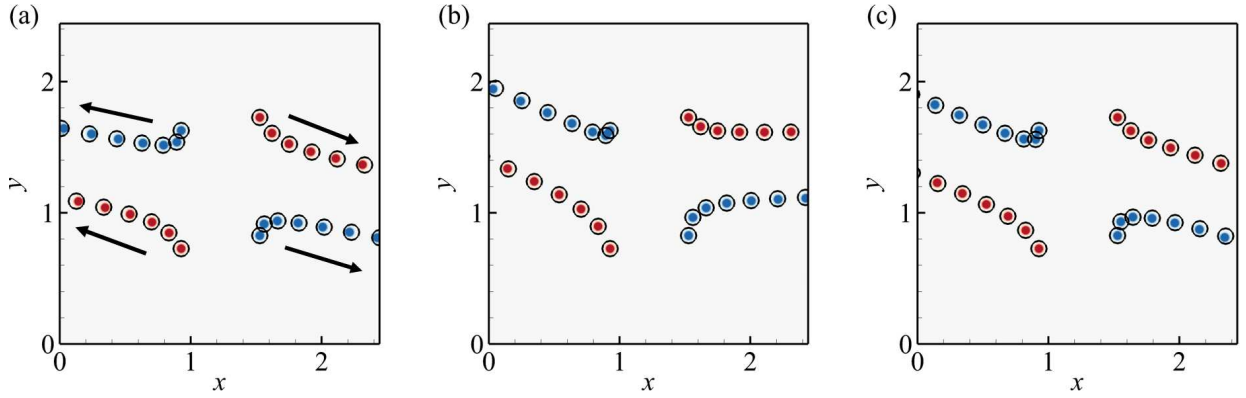


Figure 7: Prediction results using NVM for three cases with (a) $\mathbf{f} = \mathbf{0}$, (b) $\mathbf{f} = 0.05\omega(1,0)$, and (c) $\mathbf{f} = 0.02\omega(\cos(x - x_c), -\sin(y - y_c))$. The black arrows indicate the directions of the motions of the 2 vortices. ω represents the vorticity, and (x_c, y_c) is the center of the computation domain.

plot the results generated by CVM, because CVM is incapable of solving the fluid dynamics with non-zero external forces, since it fails to capture the drift velocity \mathbf{v}_i caused by the external force.

4 Related work

Computational fluid dynamics In the field of computational fluid dynamics (CFD), numerical analysis and data structures are used to analyze and solve the motions of fluid flows. Two general approaches are developed to achieve this task, one is grid-based, or Eulerian, and the other is particle-based, or Lagrangian. Conventionally, many pieces of research are done on grid-based methods mainly to achieve high resolution, for example on channel flow [20, 50], boundary layers [40, 33], isotropic turbulence [16, 18, 17], and pipe flow [39]. However, the main drawback of grid-based methods is their high computational cost that is unaffordable under many conditions. On the contrary, the particle-based approach is efficient in computation but suffers from inaccuracy in results [24, 25]. CVMs are well-known particle-based methods, which use vortices as the computational elements, mimicking the physical structures

in turbulence. In CVMs, the Euler equations are formulated in terms of vorticity in contrast to the conventional formulations with velocity and pressure and are solved using a Lagrangian approach instead of the Eulerian formulation [22, 7, 1].

Machine learning in fluid systems The rapid advent of machine learning techniques is opening up new possibilities to solve the physical system’s identification problems by statistically exploring the underlying structure of a variety of physical systems, encompassing applications in quantum physics [35], thermodynamics [14], material science [36], rigid body control [9], Lagrangian systems [8], and Hamiltonian systems [10, 19, 37]. Specifically, in the field of fluid mechanics, machine learning offers a wealth of techniques to extract information from data that could be translated into knowledge about the underlying fluid field, as well as exhibits its ability to augment domain knowledge and automate tasks related to flow control and optimization [4, 11]. Recently, many pieces of research are developed to efficiently learn the fluid dynamics through incorporating physical priors into the learning framework, e.g., encoding the Navier-Stokes equations [29], embedding the notion of an incompressible fluid [28], and identifying a mapping between the dynamics of wave-based physical phenomena and the computation in a recurrent neural network (RNN) [15].

Learning physics laws from high dimensional observations One of the key strengths of neural networks is that they can learn abstract representations directly from high-dimensional data such as pixels. With the advances of image detection techniques [13, 31], it is natural to apply these techniques to better learn and predict physical phenomena. Belbute-Peres et al., attempted to learn a model of physical system dynamics end-to-end from image sequences using an autoencoder [3]. Greydanus et al., also tried to combine an autoencoder with an Hamiltonian Neural Networks (HNN) to model the dynamics of pixel observations of a pendulum [10]. Toth et al., later developed Hamiltonian Generative Network (HGN), which is capable of consistently learning Hamiltonian dynamics from high-dimensional observations without restrictive domain assumptions [38]. Some related works done on fluid dynamics include Hidden Fluid Mechanics (HFM) by Raissi et al., [30]. However, HFM differs from our work by learning the underlying governing function purely based on the Eulerian grid.

5 Conclusion

This paper presented NVM, a novel learning-based framework, which builds a neural-network description of the Lagrangian vortex structures and their interaction dynamics to reconstruct the high-resolution Eulerian flow field in a physically-precise manner. We demonstrated the efficacy of our method in generating highly accurate prediction results, with low computational cost, of the leapfrogging vortex rings system, the turbulence system, and the systems governed by Euler equations with different external forces. We compared the prediction results made by NVM and CVM for solving Euler equation in the periodic box and discovered that the relative error of predict velocity using NVM is more than 10 times smaller than that of CVM. Moreover, our method only requires training data collected from a very short window of training period (more than 100 times shorter than the prediction period), which will potentially solve data acquisition problems in real systems. Our method is the first approach that can utilize motions of finite particles to learn infinite dimensional dynamic systems. Featured by its unique ability to generate highly accurate prediction results with low computational, NVM marks a significant advancement in numerical fluid simulation.

6 Broader Impact

Accurately capturing and quantifying the motions of fluid has been a long-standing subject in the study of fluid dynamics, embracing a broad application in fields, such as fluid mechanics, wave physics, thermodynamics, quantum physics, aerodynamic, geophysics, electromagnetics, engineering and biomedicine. Our method, highlighted by its ability to generate highly accurate prediction results with low computational cost, marks a critical improvement in numerical fluid simulation. Moreover, our method only requires training data collected from a very short window of training period (more than 100 times shorter than the prediction period), which will potentially solve data acquisition problems in real systems. This research does not bring any direct ethical consequence, but the application of our method to fields like biomedicine can potentially cause ethical issues.

References

- [1] C. Anderson and C. Greengard. On vortex methods. *SIAM J.Numer. Anal.*, 22:413–440, 1985.
- [2] P. Battaglia, R. Pascanu, M. Lai, and D. J. Rezende. Interaction networks for learning about objects, relations and physics. In *Advances in neural information processing systems*, pages 4502–4510, 2016.

- [3] de A. F. Belbute-Peres, A. K. Smith, K. Allen, J. Tenenbaum, and Z. J. Kolter. End-to-end differentiable physics for learning and control. In *Advances in neural information processing systems*, pages 7178–7189, 2018.
- [4] S. L. Brunton, B. R. Noack, and P. Koumoutsakos. Machine Learning for Fluid Mechanics. *Annu. Rev. Fluid Mech.*, 52:477–508, 2020.
- [5] N. Chentanez and M. Müller. Real-time Eulerian water simulation using a restricted tall cell grid. *ACM Trans. Graph.*, 30:4, 2011.
- [6] A. Chern, F. Knöppel, U. Pinkall, P. Schröder, and S. Weißmann. Schrödinger’s smoke. *ACM Trans. Graph.*, 35:77, 2016.
- [7] G.H. Cottet and P.D. Koumoutsakos. *Vortex Methods: Theory and Practice*. Cambridge University Press, 2000.
- [8] M. Cranmer, S. Greydanus, S. Hoyer, P. Battaglia, D. Spergel, and S. Ho. Lagrangian neural networks. *arXiv:2003.04630*, 2020.
- [9] Z. Geng, D. Johnson, and R. Fedkiw. Coercing machine learning to output physically accurate results. *J. Comput. Phys.*, 406:109099, 2020.
- [10] S. Greydanus, M. Dzamba, and J. Yosinski. Hamiltonian neural networks. In *Advances in Neural Information Processing Systems*, pages 15379–15389, 2019.
- [11] Philipp H., Nils T., and Vladlen K. Learning to Control PDEs with Differentiable Physics. In *International Conference on Learning Representations*, 2020.
- [12] J. Hao, S. Xiong, and Y. Yang. Tracking vortex surfaces frozen in the virtual velocity in non-ideal flows. *J. Fluid Mech.*, 863:513–544, 2019.
- [13] K. He, X. Zhang, S. Ren, and J. Sun. Deep residual learning for image recognition. In *Proceedings of the IEEE conference on computer vision and pattern recognition*, pages 770–778, 2016.
- [14] Q. Hernandez, A. Badias, D. Gonzalez, F. Chinesta, and E. Cueto. Structure-preserving neural networks. *arXiv:2004.04653*, 2020.
- [15] T. W. Hughes, I. A. D. Williamson, M. Minkov, and S. Fan. Wave physics as an analog recurrent neural network. *Sci. Adv.*, 5:6946, 2019.
- [16] T. Ishihara, K. Morishita, M. Yokokawa, A. Uno, and Y. Kaneda. Energy spectrum in high-resolution direct numerical simulations of turbulence. *Phys. Rev. Fluids*, 1:082403, 2016.
- [17] J. Jimenez and A. A. Wray. The structure of intense vorticity in isotropic turbulence. *J. Fluid Mech.*, 373:255–285, 1993.
- [18] J. Jimenez, A. A. Wray, P. G. Saffman, and R. S. Rogallo. The structure of intense vorticity in isotropic turbulence. *J. Fluid Mech.*, 255:65–90, 1993.
- [19] P. Jin, A. Zhu, G. E. Karniadakis, , and Y. Tang. Symplectic networks: Intrinsic structure-preserving networks for identifying Hamiltonian systems. *arXiv:2001.03750*, 2020.
- [20] J. Kim, P. Moin, and R. D. Moser. Turbulent statistics in fully developed channel flow at low Reynolds number. *J. Fluid Mech.*, 177:133–166, 1987.
- [21] D. P. Kingma and J. Ba. Adam: A method for stochastic optimization. *arXiv:1412.6980*, 2014.
- [22] A. Leonard. Vortex methods for flow simulation. *J. Comput. Phys.*, 37:289–335, 1980.
- [23] T. Lin, P. Goyal, R. Girshick, K. He, and P. Dollár. Focal loss for dense object detection. *IEEE Trans. Vis. Comput. Graph.*, pages 2980–2988, 2017.
- [24] K. Lindsay and R. Krasny. A particle method and adaptive treecode for vortex sheet motion in three-dimensional flow. *J. Comput. Phys.*, 172:879–907, 2001.
- [25] F. Losasso, J. Talton, N. Kwatra, and R. Fedkiw. Two-way coupled sph and particle level set fluid simulation. *IEEE Trans. Vis. Comput. Graph.*, 14:797–804, 2008.
- [26] T. S. Lundgren. Strained spiral vortex model for turbulent fine structure. *Phys. Fluids*, 25:2193–2203, 1982.
- [27] T. S. Lundgren. A small-scale turbulence model. *Phys. Fluids A*, 5:1472, 1993.
- [28] A. T. Mohan, N. Lubbers, D. Livescu, and M. Chertkov. Embedding hard physical constraints in convolutional neural networks for 3D turbulence. In *International Conference on Learning Representations*, 2020.
- [29] M. Raissi and G. E. Karniadakis. Hidden physics models: Machine learning of nonlinear partial differential equations. *J. Comput. Phys.*, 357:125–141, 2018.

- [30] M. Raissi, A. Yazdani, and G. E. Karniadakis. Hidden fluid mechanics: Learning velocity and pressure fields from flow visualizations. *Science*, 367(6481):1026–1030, 2020.
- [31] J. Redmon, S. Divvala, R. Girshick, and A. Farhadi. You only look once: Unified, real-time object detection. In *Proceedings of the IEEE conference on computer vision and pattern recognition*, pages 779–788, 2016.
- [32] R. S. Rogallo. Numerical experiments in homogeneous turbulence. In *Technical Report TM81315, NASA*, 1981.
- [33] T. Sayadi, C. W. Hamman, and P. Moin. Direct numerical simulation of complete H-type and K-type transitions with implications for the dynamics of turbulent boundary layers. *J. Fluid Mech.*, 724:480–509, 2013.
- [34] A. Selle, N. Rasmussen, and R. Fedkiw. A vortex particle method for smoke, water and explosions. *ACM Trans. Graph.*, 3:910–914, 2005.
- [35] J. M. Sellier, G. M. Caron, and J. Leygonie. Signed particles and neural networks, towards efficient simulations of quantum systems. *J. Comput. Phys.*, 387:154–162, 2019.
- [36] G. H. Teicherta, A. R. Natarajanc, A. Van der Venc, and K. Garikipati. Machine learning materials physics: Integrable deep neural networks enable scale bridging by learning free energy functions. *Comput. Methods Appl. Mech. Engrg.*, 353:201–216, 2019.
- [37] Y. Tong, S. Xiong, X. He, G. Pan, and Bo Z. Symplectic neural networks in Taylor series form for Hamiltonian systems, 2020.
- [38] P. Toth, D. J. Rezende, A. Jaegle, S. Racanière, A. Botev, and I. Higgins. Hamiltonian generative networks. In *International Conference on Learning Representations*, 2020.
- [39] X. Wu, P. Moin, R. J. Adrian, and J. R. Baltzer. Osborne Reynolds pipe flow: Direct simulation from laminar through gradual transition to fully developed turbulence. *Proc. Natl. Acad. Sci. U.S.A.*, 112:7920–7924, 2015.
- [40] X. Wu, P. Moin, J. M. Wallace, J. Skarda, A. Lozano-Durán, and J. Hickey. Transitional–turbulent spots and turbulent–turbulent spots in boundary layers. *Proc. Natl. Acad. Sci. U.S.A.*, 114:E5292–E5299, 2017.
- [41] S. Xiong and Y. Yang. The boundary-constraint method for constructing vortex-surface fields. *J. Comput. Phys.*, 339:31–45, 2017.
- [42] S. Xiong and Y. Yang. Construction of knotted vortex tubes with the writhe-dependent helicity. *Phys. Fluids*, 31:047101, 2019.
- [43] S. Xiong and Y. Yang. Identifying the tangle of vortex tubes in homogeneous isotropic turbulence. *J. Fluid Mech.*, 874:952–978, 2019.
- [44] S. Xiong and Y. Yang. Effects of twist on the evolution of knotted magnetic flux tubes. *J. Fluid Mech.*, 895:A28, 2020.
- [45] Y. Yang and D. I. Pullin. Geometric study of Lagrangian and Eulerian structures in turbulent channel flow. *J. Fluid Mech.*, 674:67–92, 2011.
- [46] Y. Yang, D. I. Pullin, and I. Bermejo-Moreno. Multi-scale geometric analysis of Lagrangian structures in isotropic turbulence. *J. Fluid Mech.*, 654:233–270, 2010.
- [47] Y. Zhao, Y. Yang, and S. Chen. Evolution of material surfaces in the temporal transition in channel flow. *J. Fluid Mech.*, 793:840–876, 2016.
- [48] W. Zheng, S. Ruan, Y. Yang, L. He, and S. Chen. Image-based modelling of the skin-friction coefficient in compressible boundary-layer transition. *J. Fluid. Mech.*, 875:1175–1203, 2019.
- [49] W. Zheng, Y. Yang, and S. Chen. Evolutionary geometry of Lagrangian structures in a transitional boundary layer. *Phys. Fluids*, 28:035110, 2016.
- [50] J. Zhou, R. J. Adrian, S. Balachandar, and T. M. Kendall. Mechanisms for generating coherent packets of hairpin vortices in channel flow. *J. Fluid Mech.*, 387:353–396, 1999.